ELSEVIER

Contents lists available at ScienceDirect

Infrared Physics & Technology

journal homepage: www.elsevier.com/locate/infrared



InSb pixel loaded microwave resonator for high-speed mid-wave infrared detection



Yinan Wang^a, Sukrith Dev^a, Frank Yang^b, Leland Nordin^a, Yimeng Wang^a, Andrew Briggs^a, Monica Allen^c, Jeffery Allen^c, Emanuel Tutuc^a, Daniel Wasserman^{a,*}

- ^a Electrical and Computer Engineering, Microelectronics Research Center, University of Texas at Austin, Austin, TX 78758, USA
- ^b Electrical and Computer Engineering, Rice University, Houston, TX 77005, USA
- ^c Air Force Research Laboratory, Munitions Directorate, Eglin Air Force Base, Eglin AFB, FL 32542, USA

ARTICLE INFO

Keywords: High-speed detection Infrared detection Microwave photonics

ABSTRACT

High-speed mid-wave infrared (MWIR) detectors are of significant interest for a wide range of applications in communication and spectroscopy. High-speed photodetection is conventionally achieved using reverse biased semiconductor p-i-n junction devices. However, implementing such structures in the mid-infrared (mid-IR) is challenging due to both the limited available material platforms and challenges associated with device design. Here we demonstrate a high-speed MWIR detector architecture that uses a microwave resonator circuit loaded with a photoconductive indium antimonide (InSb) pixel, originally grown highly lattice-mismatched on a GaAs substrate. Time domain measurements demonstrate sub-nanosecond detector response at temperatures from 77 K to room temperature. Frequency response measurements demonstrate that optical signals modulated at frequencies as high as 2 GHz can be well resolved up to room temperature. Time domain circuit simulations support the experimentally measured short minority carrier lifetimes in the InSb pixel, while also suggesting a circuit time constant of ~200 ps, which is ultimately the limiting factor for the bandwidth of the presented detector architecture. Our results provide an alternative approach for the development of contact-free, high-speed infrared detectors capable of directly interfacing with microwave components and structures for a range of RF/mid-IR applications.

1. Introduction

Infrared detection is vital for a number of applications such as imaging, free space communication, sensing, and spectroscopy [1-4]. Many of these applications could benefit greatly from sensitive infrared detectors capable of high-speed operation. As a particularly intuitive example, detector response times could serve as a limiting factor for the bandwidth of infrared free space communication systems. High-speed detectors are, at the same time, becoming an increasingly important factor in the rapid development of novel sensing and spectroscopy techniques where the time resolution of current detectors is a bottleneck for the exploration of ultrafast phenomena and events in the mid-IR. In the case of dual-comb spectroscopy (DCS) [3] an infrared frequency comb, namely a coherent IR source consisting of discrete and equally spaced optical frequency lines, is combined with a second comb operating in same optical frequency range, but with slightly different comb spacing. The two sources are combined on a high-speed detector, and the resulting detector signal will consist of the radio frequency (RF)

beat notes between the discrete lines of the two laser sources. If one or both of these sources passes through an absorbing material, the frequency lines overlapping with the material absorption feature will be attenuated, as will the RF beat notes associated with the attenuated optical frequencies, essentially mapping the optical absorption spectrum to the RF spectrum. Thus, a technique such as DCS offers broad band, high resolution, and high sensitivity spectroscopic capabilities with direct electrical read-out at RF frequencies. Mid-IR frequency combs [5–8] and DCS systems [9–14] have been demonstrated in multiple studies, and there is growing interest in developing high-speed, low noise, and high sensitivity IR detectors to serve as detectors/mixers for future DCS applications [11–16].

High-speed infrared detection has been demonstrated with multiple material systems and detector architectures. The predominant material used in mid- and long-wave infrared detection, mercury cadmium telluride (MCT), has been integrated into photovoltaic detectors which have achieved GHz-level cutoff frequency [17]. Alternatively, p-i-n junction detectors have been fabricated with the narrow bandgap III-V

E-mail address: dw@utexas.edu (D. Wasserman).

^{*} Corresponding author.

material, indium antimonide (InSb), and show detectivity comparable with, and higher bandwidth than, high-speed MCT detectors [18]. Quantum well infrared photodetectors (QWIPs) and quantum dot infrared photodetectors (QDIPs) are also candidates for high-speed infrared detection due to their extremely short carrier recombination/ relaxation times [19-23]. However, most, if not all, of the existing highspeed IR detector demonstrations require the collection of photo-generated carriers through a direct electrical contact to the absorber material. For high-speed operation in the RF regime, the design of electrical contacts that efficiently transmit the photo-generated signal to the read-out circuit becomes non-trivial. Adding to the challenge of highspeed IR detector development is the fact that the area of the detecting element often has to be kept small in order to reduce the detector RC time constant, which also introduces tradeoffs between detector sensitivity and operational speed. Therefore, a contact-free, RF-compatible detector architecture could be highly desirable for the development of high sensitivity, high-speed mid-IR photodetectors.

In this work, we demonstrate a high-speed mid-wave infrared (MWIR, 3-5 µm) detector using a reactively coupled loaded RF resonator detection architecture [24-26]. A split-ring-resonator (SRR) is coupled to a microstrip busline. When driven at the resonant frequency, the RF wave couples into the SRR and results in an attenuated RF transmission. A photoconductive semiconductor absorber material is loaded in the gap of the SRR, where most of the RF fields are confined when driven on resonance. The light-sensitive absorber provides a mechanism for optically modulating the resonance of the RF circuit. A schematic of the detector architecture is shown in Fig. 1. The device is normally operated at the resonant frequency of the SRR. Light absorbed by the pixel generates electron-hole pairs, which alter the conductivity of the pixel and change the resonance of the SRR. This further causes a change in the amplitude of the transmitted RF signal on the busline, which can be used as a readout for the input optical signal. While the development of infrared detection has been largely driven by imaging applications, where an array of detectors is required, for emerging applications such as dual-comb spectroscopy and infrared ranging, the signal from a single element detector is used to extract the desired information and high speed detection is paramount. With this in mind, in this work we demonstrate a single element detector, targeting a fast response time, although sparse linear detector arrays on a single busline can also be achieved with this architecture [24] for applications requiring multiple simultaneous signals via multiplexed read-out. Previous work [26] has also indicated that such reactively coupled detector architectures can intrinsically possess lower Johnson noise than direct current (DC)-based architectures, resulting in improved detectivity (D*) when compared to the same absorbing element operated in a conventional DC-biased photoconductive architecture. When operated in this manner, the output of the circuit is rectified by an RF detector, a Schottky diode, and the ensuing quasi-DC signal provides a straightforward measure of the light incident upon the pixel. However, such an architecture should also be able to read out IR signals modulated at RF frequencies, such as those coming from the beat notes generated in dual-comb spectroscopy. In this case, the optical signal incident upon the photoconducting pixel would be mixed with the driving RF carrier signal, with the optical modulation reading out as sidebands on the resonant carrier frequency, in the frequency domain. Thus, the detector architecture presented in this work not only offers direct RF frequency read-out, but if properly designed, the opportunity for high bandwidth operation. The bandwidth of this detector architecture is determined by the transient response of the circuit itself and the carrier lifetime of the material. The circuit response time can be considered as the time constant associated with the resonator response to a change in the driving signal amplitude (which will be related to the quality factor Q of the resonator). For the relatively high frequency ($f_0 \sim 16.5$ GHz), low-Q resonators (Q < 10) employed in the presented detector architecture, the circuit time constant will be on the order of ~ 100 's of ps. On the material side, the minority carrier lifetime (τ), or the average time before a photo-excited electron hole pair recombines, is the time constant associated with the change in the pixel conductivity due to a change in infrared illumination. The key to realizing a sensitive and high-speed, resonator-response-limited detector is thus to combine the SRR with an absorber material that has a fast carrier recombination lifetime.

Here, epitaxial InSb grown lattice-mismatched on GaAs substrates is chosen as the absorbing material. The large lattice mismatch between InSb and GaAs will result in a large defect density in the epitaxial InSb [27], leading to fast recombination times, while still offering strong interband infrared absorption. In conventional detector architectures, where the signal consists of a collected photocurrent, a large defect density can lead to rapid recombination of photo-excited charge carriers, before they are able to be collected as an electrical signal,

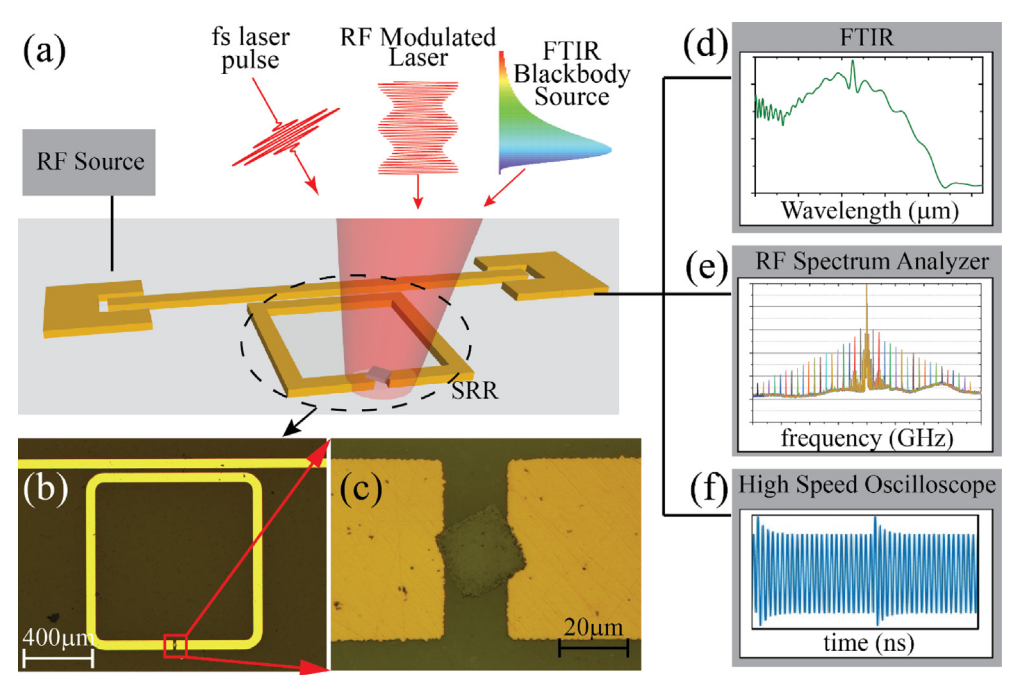


Fig. 1. Overview of the device architecture and experimental setups. (a) A radiofrequency (RF) source is used to drive the split-ring-resonator (SRR) at resonant frequency. The infrared absorbing semiconductor pixel is placed in the gap of the SRR, as shown in optical microscope images (b) and (c). The device is characterized using three different set of optical sources and detection instruments. (d) To obtain optical absorption spectra, broadband light from a blackbody source of a Fourier transform infrared (FTIR) spectrometer is used, with the RF circuit output fed back into the FTIR. (e) The frequency response of the detector is measured using an RF-modulated continuous wave (CW) laser with the circuit output sent to an RF spectrum analyzer. (f) The detector time response is characterized using a femtosecond pulsed laser to excite carriers in the InSb pixel. The decay of the photo-generated carriers is measured with a high-speed digital sampling oscilloscope.

therefore reducing detector responsivity. However, in the RF architecture presented in this work, the photo-generated carriers are not collected in the form of a current. Instead, they are instantaneously probed by the overlapping RF field, confined in the vicinity of the pixel by the resonator, allowing us to take advantage of the fast recombination times to achieve high-speed detector operation. Individual free-standing pixels of this InSb material are fabricated [28] and transferred [29] to the gap of the SRR. The detector's optical absorption spectrum, time response and RF modulation response are characterized, as shown schematically in Fig. 1. The time response data and analysis show that this detector has a sub-nanosecond time constant. Even at room temperature, response to RF modulated light is resolvable up to modulation frequencies as high as 2 GHz. In addition to demonstrating detection of high frequency signals, this detector architecture also has the advantage of direct RF read-out, which could be important for integration into communication or spectroscopy systems operating at microwave frequencies.

2. Methods

2.1. Material preparation

The absorber material used in this work is grown by molecular beam epitaxy (MBE) and consists of a 600 nm InSb layer grown on top of a 200 nm AlSb sacrificial layer on a semi-insulating GaAs wafer. The large lattice mismatch between AlSb/InSb and GaAs (~14%) will cause significant defects which will degrade carrier lifetime [27] and, thus, increase detector speed. In order to fabricate the pixels, we begin with the as-grown AlSb/InSb epilayer, and then etch mesas down to the GaAs substrate by inductively coupled plasma (ICP) dry etching (BCl₃, Cl₂ and Ar gases [30]) using a photoresist etch mask defined by UV photolithography. We then use a 40-min diluted HF (HF: H₂O = 1:1000) bath to selectively etch the sacrificial AlSb layer so that the InSb pixel is supported by a ~10 μ m diameter AlSb pillar. A PDMS stamp is used to peel the pixels from the original substrate [28]. The average pixel size following the dry etch and undercut is 21 \times 21 μ m.

The SRR is fabricated on a 500 μm -thick 99.6% aluminum oxide substrate using a standard lithography, metallization (10 nm Ti followed by 500 nm Au), and lift-off process. The SRR microstrip width is 50 μm , the side length is 1 mm, and the split-gap is 20 μm . The SRR is coupled to a 50 μm wide microstrip busline via a 30 μm wide coupling gap. The microstrip busline is terminated on both ends with coplanar contact pads. The InSb pixel is then transferred to the SRR using a pick-and-place dry transfer technique [29]. We fabricate and test four devices with four pixels randomly chosen from the PDMS stamp, all show similar responsivities and response times.

2.2. Experimental setups

The detector absorption spectra are measured using a Fourier transform infrared (FTIR) spectrometer operated in amplitude modulation step-scan mode. The sample is placed in a temperature-controlled closed-looped cryogenic probe station for temperature-dependent spectral response measurements. Mid-IR light from the FTIR is modulated using an optical chopper at 1 kHz and focused down onto the sample using free-space optics. The sample is driven with an RF source at the resonance frequency and 1 dBm of input RF power. The RF output from the sample is rectified by a Schottky diode RF detector, amplified by a preamplifier, and sent to a lock-in amplifier (LIA), referenced to the chopper frequency. The output of the LIA is fed back to the FTIR. To normalize out the response function of the FTIR source and optics, the spectra are divided by a reference spectrum measured with a spectrally flat pyroelectric detector.

The temperature- and power-dependent time response of the device is characterized by exciting the loaded pixel with a pulsed 1550 nm laser, operated with a 20 MHz repetition rate and pulse widths of

~100 fs. The pulse energy is controlled using neutral density filters. The sample, placed in the cryo-probe station, is driven at the SRR resonance frequency with 12 dBm of RF power. The circuit output is sent directly to a high-speed digital sampling oscilloscope without rectification by a Schottky diode. The synch signal from the laser is used as trigger for the oscilloscope. However, because the RF carrier signal is not synchronized with the laser pulses, the sinusoidal carrier signal measured on the scope is phase-randomized and appears as a full band of sampled points. The absorption of the laser pulse modifies the InSb pixel conductivity, resulting in a time-dependent RF transmission coefficient for the microwave circuit. The transient envelope of the transmitted RF signal is then measured by the oscilloscope, which is synchronized to the pulsed laser. From the raw data, the envelope of the temporal decay signal is obtained by separating the data into bins of n points and picking out the point with maximum amplitude from each bin. n is manually determined for each data set to extract a clean envelope.

To test the frequency-response of the detector, a continuous wave 1550 nm laser, set to a constant power and externally modulated by an electro-optical lithium niobate modulator driven by an RF source, is used to excite the pixel. The total output power and beam profile of the modulated light incident upon the detector are measured using the knife edge method. From this, the integrated laser power over the pixel is found to have a 200 μW modulation amplitude over a CW power of 300 μW . The modulated laser power shows no significant fluctuations with regard to the modulation frequency in the range we tested (0–3 GHz). A second RF source is used to drive the detector circuit at resonance with 12 dBm RF power. The output from the detector circuit is measured with an RF spectrum analyzer.

3. Results and discussions

The temperature-dependent spectral response of the detector is shown in Fig. 2, and as would be expected for InSb, shows a low temperature ($T=77~\rm K$) cut-off wavelength of $\lambda\sim5.6~\rm \mu m$, extending to longer wavelengths at elevated temperature ($T=275~\rm K$). At room temperature ($T=300~\rm K$), for an RF driving power of 1 dBm, the detector response to the broadband, weak FTIR source illumination is below the noise floor of our measurement system. The fluctuations in the absorption spectra at $\lambda\sim4.2~\rm \mu m$ are due to atmospheric fluctuations in CO₂ absorption between experiments. The decrease in our detector response with increasing temperature is attributed to increased background carrier concentration in the pixel, which decreases the resonator Q and, thus, reduces the contrast between dark and illuminated state, effectively the RF equivalent of increased dark current.

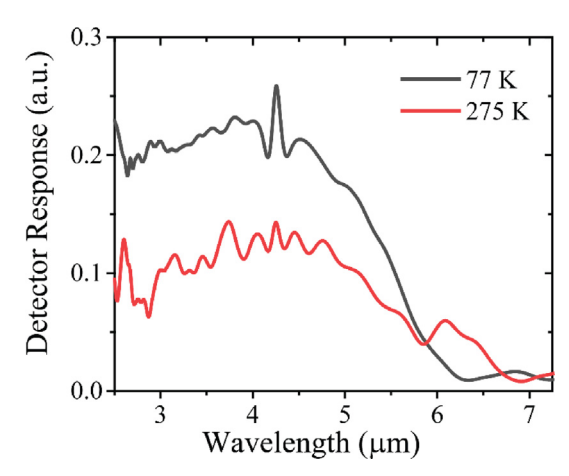


Fig. 2. Detector response spectra at 77 K and 275 K. The optical transfer functions of the IR source and the optics in the FTIR beam path are normalized out by dividing the raw RF-detector spectra by the spectrum of the light incident upon the detector, as measured by a reference pyroelectric detector with flat spectral response.

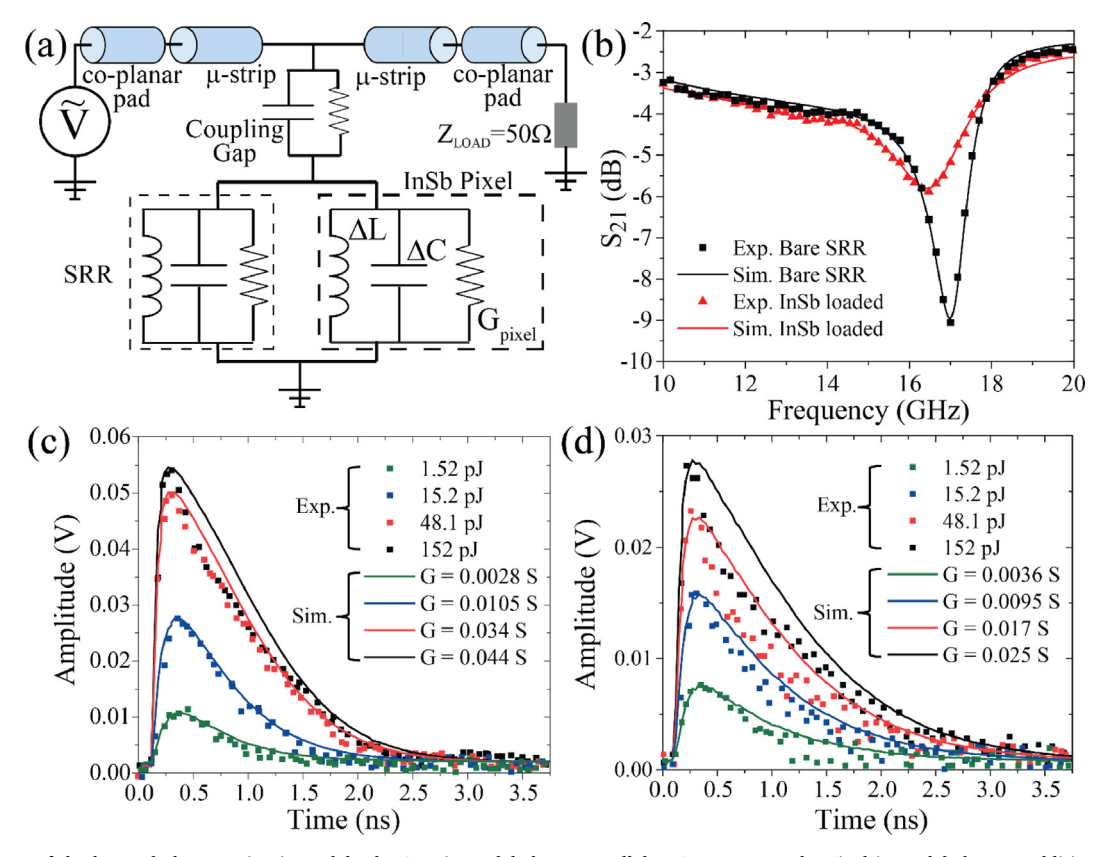


Fig. 3. (a) Diagram of the lumped element circuit model. The SRR is modeled as a parallel RLC resonator. The pixel is modeled as an additional parallel RLC in parallel with the SRR. (b) Measured and simulated S_{21} parameters before and after pixel transfer. (c and d) Measured and simulated time responses of the device to pulsed optical excitation of varying pulse energies at (c) 77 K and (d) 300 K. Legends for the experimental data sets denote the optical energy incident on the pixel. Legends for the simulated curves denote the extracted value for the fitting parameter G. The extracted fitting parameters are (c) $G_0 = 0.0024S$, $\tau = 0.46ns$ for T = 77 K and (d) $G_0 = 0.008S$, $\tau = 0.7$ ns for T = 300 K. Note that the scales differ by a factor of two between (c) 77 K and (d) 300 K.

Because the carrier lifetime in the material is expected to be of the same order of magnitude as the time constant of the circuit, estimated to be ~100's of ps, the measured temporal decay envelope is a combined response of both the circuit response and the recombination lifetime in the material. Therefore, a conventional single exponential fit to the decay envelope may not be applicable in this situation. Here, we use a lumped element circuit model to simulate the device time response signal and extract a carrier lifetime value. The circuit is modeled using an open source software [31], both in the frequency and time domain. As shown in the circuit diagram in Fig. 3(a), the SRR is modeled as a parallel RLC resonator, and the loaded pixel is modeled as additional conductance, capacitance and inductance G_{pixel} , ΔL , and ΔC in parallel with the RLC resonator. Frequency domain simulations are used to obtain the dark state values of circuit components by fitting the simulated frequency response to the experimental S_{21} parameters, measured with a vector network analyzer calibrated to the probe plane and shown in Fig. 3(b). The fitted component values are then used in the time domain simulations, where the circuit is driven with a single sinusoidal wave at the resonant frequency, and a time-varying value is assigned to G_{pixel} to simulate the change in the conductivity of the pixel upon optical excitation,

$$G_{pixel} = G_0 + G \exp\left(-\frac{(t - t_0)}{\tau}\right) \tag{1}$$

where G_0 is the dark state pixel conductance obtained from the frequency domain simulation and fitting, G is the photo-generated change in conductance, t_0 is the time delay of the optical pulse, and τ is the effective carrier recombination time constant. G and τ are tuned to fit the simulated result to the measured time response envelope.

The experimentally measured detector time responses, as a function

of pump pulse energy, are shown in Fig. 3(c) and (d), for 77 K and 300 K respectively. The simulated time responses are shown as well, with the extracted fitting parameter G. In the simulations, τ and G are chosen to fit the tail of the time response while also matching the peak amplitude. At the lowest pump energies, the simulated response curves fit the experimental data well over the entire time window. For increasing pump energies, discrepancies can be seen between the measured and simulated time response. Firstly, the measured responses at increasing pump energies have faster initial decays when compared with the corresponding simulations. Secondly, the extracted values for G do not scale linearly with the pump energies in the experiments. Both of these effects are consistent with Auger recombination, a well-known challenge for optoelectronic devices utilizing narrow-band gap III-V semiconductors such as InSb [32]. Auger recombination results in a carrier-concentration-dependent, thus time-dependent, carrier recombination lifetime, which agrees with the faster initial decays seen in the experimental data at higher pump energies and temperatures. Additionally, because the single- τ model used in the simulations underestimates the initial decay rate, it further leads to an underestimation of G and thus contributes to the nonlinear scaling of G with the pump energies. These effects are also more prominent at both higher temperatures and higher pump energies, as would be expected for Auger recombination related effects. Although the integration of Auger recombination effects is required in order to model the time responses at high pump energies more accurately, the simple model employed here yields accurate fits to the data at low pump energy, which corresponds to low optical injection that is consistent with typical detector operation regimes. Moreover, the discrepancies between our simulations and data at higher pump energies provide insight into possible mechanisms which could degrade detector performance in specific experimental systems, such as dual-comb spectroscopy. Using the single- τ fitting process, we extract time constants $\tau=0.46$ ns at 77 K and $\tau=0.7$ ns at 300 K. The extracted time constants remain below 1 ns across the entire temperature range investigated (11–300 K). Thus, even fitting to the tail of our response results in sub-nanosecond detector response times at all measured temperatures. Interestingly, the fitted τ are seen to be increasing with increasing temperature, suggesting that the observed lifetimes might ultimately be determined by trap assisted recombination [33], which would be expected given the highly lattice mismatched growth.

Using our lumped element time-domain model, and setting $\tau \to 0$, we can minimize the contributions from the material and investigate the theoretical circuit-limited transient response of the device. This simulation gives a decay time constant of $\tau_{ckt}=208.6\,$ ps, consistent with the circuit response time estimated using the circuit resonant frequency and quality factor. This time constant predicts the ultimate frequency response limit associated with the SRR structure. The model shows that further increasing detector speed requires both materials with faster lifetimes and improvements in the circuit design. Nevertheless, the material lifetime is currently the dominant limiting factor for detector speed. Materials with lifetimes faster than the circuit time constant are required to push the detector speed towards the circuit response limit.

The modulation response spectra of the detector measured using an RF spectrum analyzer are shown in Fig. 4. When the incident light is modulated at a frequency f_{mod} , the amplitude of the RF carrier signal is modulated at this same frequency, leading to frequency mixing between the carrier frequency and the modulation frequency. When measured on a spectrum analyzer, a pair of spectral features located at frequencies of $f_{drive} \pm f_{mod}$ are observed, the result of frequency mixing, as seen in Fig. 4(a) and (c). Additional lines, independent of modulation frequency, can be seen in all of the data presented in Fig. 4, which are found to be residual components intrinsic to the RF source driving the

device. Note that for $f_{mod} > 1.8\,$ GHz, the center frequency and frequency span of the spectrum analyzer are shifted to reduce acquisition time. Therefore, only the $f_{drive} - f_{mod}$ component is recorded. The frequency dependence of the response depends on a combination of the material response (recombination) time and the frequency dependent RF transmission of the resonator. In addition to the two main sidebands at $f_{drive} \pm f_{mod}$, higher order components at $f_{drive} \pm 2f_{mod}$ can also be observed. These sidebands are due to the nonlinear response of the detector, which we first observe in the power-dependent time response measurements shown in Fig. 3. For all RF spectra we observe a sideband suppression ratio of >15 dB. Although this nonlinearity is relatively weak, the nonlinear response would prove to be problematic for sensitive spectroscopic applications such as dual-comb spectroscopy, where the higher order (nonlinear) terms from a comb line f_n would cause crosstalk with comb line $2f_n$. The nonlinearity in the device could result from both the circuit and the material response. If the response of the resonator to a linear change in the pixel conductivity is nonlinear, the fundamental frequency sidebands $f_{drive} \pm f_{mod}$ could further mix with the modulated optical signal to generate the higher order components. This is confirmed with the circuit model by modulating G_{pixel} with a sinusoidal function. The corresponding Fourier spectrum is found to contain higher order components similar to those seen in experiments. On the material side, Auger recombination will result in a time-dependent recombination lifetime, which causes a fundamentally non-linear material response. Such nonlinearity could be reduced in the future by choosing a circuit design that avoids the use of resonators or more importantly, by replacing the InSb with absorber materials that may provide a more linear response.

Despite the limits imposed by the nonlinearity in our detector response, our detectors demonstrate resolvable response to modulation frequencies as high as $f_{mod}=2\,$ GHz, not only at low temperature, but up to room temperature. The amplitudes of the resolved high frequency

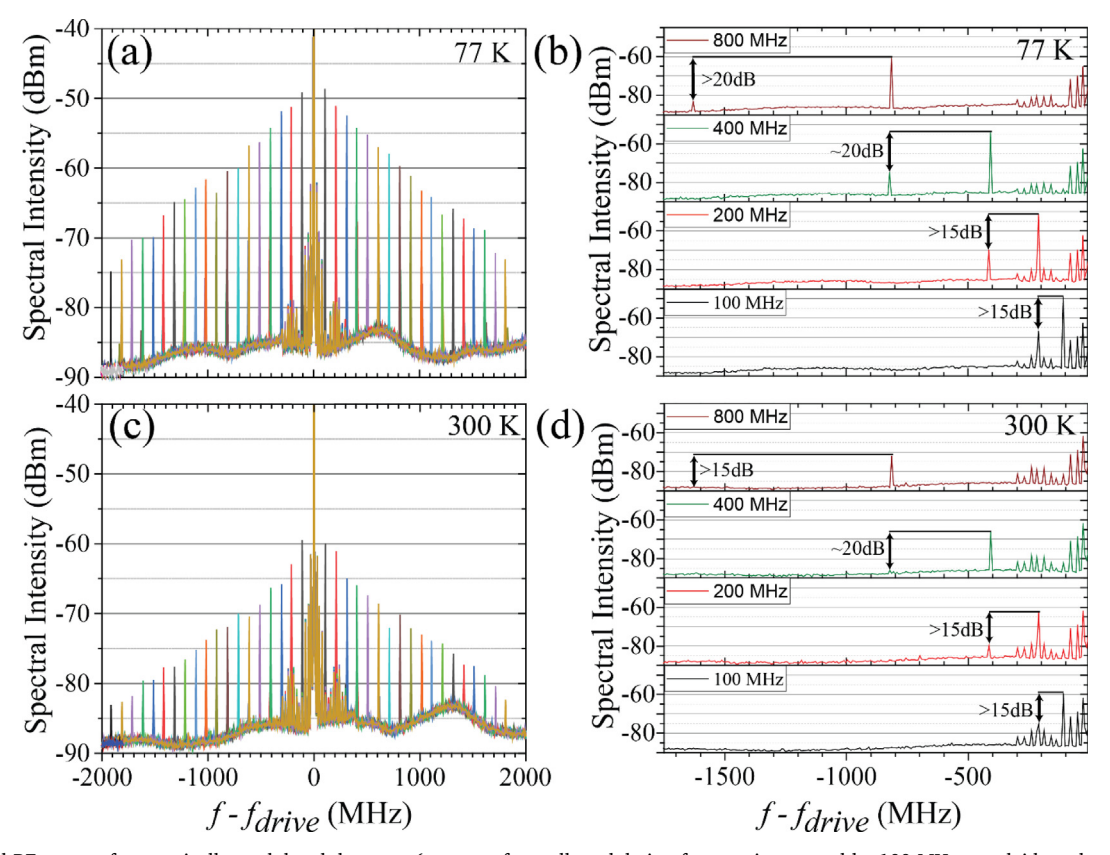


Fig. 4. Measured RF spectra from optically-modulated detectors (response from all modulation frequencies, spaced by 100 MHz, overlaid on the same plot) at (a) 77 K and (c) 300 K. Individual spectra at modulation frequencies of 100 MHz, 200 MHz, 400 MHz, and 800 MHz at (b) 77 K and (d) 300 K. The second harmonic sideband suppression ratio is shown for each of the selected modulation frequencies.

components are comparable to those observed in actual DCS systems [14]. Furthermore, the large resolvable modulation frequency range provides the headroom for reducing the repetition rate difference between the two frequency combs in DCS systems, which could increase the spectral resolution and accommodate a broader spectral region [3]. Note that such response is achieved without optimizing the microwave circuit, for example increasing metal thickness to reduce RF loss or adjusting microstrip and contact pad geometry for better impedance matching.

4. Conclusions

Utilizing a microwave resonator and exploiting an intentionally lattice mismatched grown InSb epilayer, a high-speed mid-wave infrared detector using a single micro-scale InSb pixel as the detecting element is realized. Measured time response data show a sub-nanosecond detector time response, in good agreement with time domain circuit simulations, especially for lower energy optical pulses consistent with typical IR detector operating conditions. The detector is able to resolve frequency components as high as 2 GHz at room temperature. By using microwave signal as readout, the need to collect photo-generated carriers in the form of a current is eliminated. This contact-free detection scheme provides a potential flexible platform for high-speed infrared detection. In addition, by using an RF circuit-based architecture, the detector can directly interface with RF electronic components such as spectrum analyzers, CMOS circuitry, or RF MEMS, offering opportunities for integration in advanced sensing or communication systems. Specifically, the detector architecture described has significant potential in applications that require high-speed infrared detectors for IR signals modulated at RF frequencies, such as the emerging field of dual-comb spectroscopy. The straightforward integration of alternative absorbing materials, with further reduced lifetimes, stronger absorption, or more linear response, in place of the InSb, offers a path towards extended optical bandwidth and improved detector performance. Miniaturization of the device can be achieved in the future by shifting to a high index substrate and higher operating RF frequencies, followed by an optimized geometry design and device fabrication to enhance detector response. Together with multiplexing techniques, this architecture can be expected to offer a very wide range of functionalities for emerging infrared detection applications.

Declaration of Competing Interest

The authors declare that they have no known competing financial interests or personal relationships that could have appeared to influence the work reported in this paper.

Acknowledgements

The authors MA, JA and SD would like to acknowledge funding support through the AFOSR Lab Task 20RWCOR090 (PO: Dr. M. Schmidt). The authors would like to acknowledge support from Alion Science and Technology (No. FA807519FA034), the National Science Foundation (NSF) through the Center for Dynamics and Control of Materials, an NSF MRSEC (DMR-1720595), and the use of Texas Nanofabrication Facilities supported by the NSF NNCI (EECS-1542159).

References

- R. Soref, Mid-infrared photonics in silicon and germanium, Nat. Photon. 4 (8) (2010) 495.
- [2] B. Stuart, Infrared spectroscopy, Kirk-Othmer Encyclopedia of Chemical Technology, 2000.
- [3] I. Coddington, N. Newbury, W. Swann, Dual-comb spectroscopy, Optica 3 (4) (2016) 414–426.
- [4] R. Martini, C. Bethea, F. Capasso, C. Gmachl, R. Paiella, E.A. Whittaker,

- H.Y. Hwang, D.L. Sivco, J.N. Baillargeon, A.Y. Cho, Free-space optical transmission of multimedia satellite data streams using mid-infrared quantum cascade lasers, Electron. Lett. 38 (4) (2002) 181–183.
- [5] A. Schliesser, N. Picqué, T.W. Hänsch, Mid-infrared frequency combs, Nature Photonics 6 (7) (2012) 440.
- [6] H. Guo, C. Herkommer, A. Billat, D. Grassani, C. Zhang, M.H. Pfeiffer, W. Weng, C.S. Brès, T.J. Kippenberg, Mid-infrared frequency comb via coherent dispersive wave generation in silicon nitride nanophotonic waveguides, Nature Photonics 12 (6) (2018) 330–335.
- [7] B. Meng, M. Singleton, M. Shahmohammadi, F. Kapsalidis, R. Wang, M. Beck, J. Faist, Mid-infrared frequency comb from a ring quantum cascade laser, Optica 7 (2) (2020) 162–167.
- [8] K.F. Lee, C. Mohr, J. Jiang, P.G. Schunemann, K.L. Vodopyanov, M.E. Fermann, Midinfrared frequency comb from self-stable degenerate GaAs optical parametric oscillator, Optics Exp. 23 (20) (2015) 26596–26603.
- [9] E. Baumann, F.R. Giorgetta, W.C. Swann, A.M. Zolot, I. Coddington, N.R. Newbury, Spectroscopy of the methane ν 3 band with an accurate midinfrared coherent dual-comb spectrometer, Phys. Rev. A 84 (6) (2011) 062513.
 [10] Z. Zhang, T. Gardiner, D.T. Reid, Mid-infrared dual-comb spectroscopy with an
- [10] Z. Zhang, T. Gardiner, D.T. Reid, Mid-infrared dual-comb spectroscopy with an optical parametric oscillator, Optics Lett. 38 (16) (2013) 3148–3150.
- [11] G. Villares, A. Hugi, S. Blaser, J. Faist, Dual-comb spectroscopy based on quantum-cascade-laser frequency combs, Nat. Commun. 5 (1) (2014) 1–9.
- [12] M. Yan, P.L. Luo, K. Iwakuni, G. Millot, T.W. Hänsch, N. Picqué, Mid-infrared dual-comb spectroscopy with electro-optic modulators, Light: Sci. Appl. 6 (10) (2017) e17076.
- [13] G. Ycas, F.R. Giorgetta, E. Baumann, I. Coddington, D. Herman, S.A. Diddams, N.R. Newbury, High-coherence mid-infrared dual-comb spectroscopy spanning 2.6 to 5.2 μm, Nat. Photon. 12 (4) (2018) 202–208.
- [14] M. Yu, Y. Okawachi, A.G. Griffith, N. Picqué, M. Lipson, A.L. Gaeta, Silicon-chip-based mid-infrared dual-comb spectroscopy, Nat. Commun. 9 (1) (2018) 1–6.
- [15] T. Ideguchi, S. Holzner, B. Bernhardt, G. Guelachvili, N. Picqué, T.W. Hänsch, Coherent Raman spectro-imaging with laser frequency combs, Nature 502 (7471) (2013) 355–358.
- [16] Y. Wang, M.G. Soskind, W. Wang, G. Wysocki, High-resolution multi-heterodyne spectroscopy based on Fabry-Perot quantum cascade lasers, Appl. Phys. Lett. 104 (3) (2014) 031114.
- [17] C. Verie, M. Sirieix, Gigahertz cutoff frequency capabilities of CdHgTe photovoltaic detectors at 10.6 μ, IEEE J. Quantum Electron. 8 (2) (1972) 180–184.
- [18] I. Kimukin, N. Biyikli, T. Kartaloglu, O. Aytur, E. Ozbay, High-speed InSb photodetectors on GaAs for mid-IR applications, IEEE J. Selected Topics Quantum Electron. 10 (4) (2004) 766–770.
- [19] C.G. Bethea, B.F. Levine, G. Hasnain, J. Walker, R.J. Malik, High-speed measurement of the response time of a GaAs/AlxGa1 xAs multiquantum-well long-wave length infrared detector, J. Appl. Phys. 66 (2) (1989) 963–965.
- [20] H.C. Liu, J. Li, E.R. Brown, K.A. McIntosh, K.B. Nichols, M.J. Manfra, Quantum well intersubband heterodyne infrared detection up to 82 GHz, Appli. Phys. Lett. 67 (11) (1995) 1594–1596.
- [21] D. Palaferri, Y. Todorov, A. Bigioli, A. Mottaghizadeh, D. Gacemi, A. Calabrese, A. Vasenelli, L. Li, A.G. Davies, E.H. Linfield, F. Kapsalidis, M. Beck, J. Faist, C. Sirtori, Room-temperature nine-µm-wavelength photodetectors and GHz-frequency heterodyne receivers, Nature 556 (7699) (2018) 85–88.
- [22] T. Dougakiuchi, T. Edamura, High-speed quantum cascade detector with frequency response of over 20 GHz, in: SPIE Future Sensing Technologies, vol. 11197, International Society for Optics and Photonics, 2019, November, p. 111970R.
- [23] J. Gao, S.C. Nguyen, N.D. Bronstein, A.P. Alivisatos, Solution-processed, high-speed, and high-quantum-efficiency quantum dot infrared photodetectors, ACS Photon. 3 (7) (2016) 1217–1222.
- [24] R. Liu, R. Lu, C. Roberts, S. Gong, J.W. Allen, M.S. Allen, B.R. Wenner, D. Wasserman, Multiplexed infrared photodetection using resonant radio-frequency circuits, Appl. Phys. Lett. 108 (6) (2016) 061101.
- [25] S. Dev, Y. Wang, K. Kim, M. Zamiri, C. Kadlec, M. Goldflam, S. Hawkins, E. Shaner, J. Kim, S. Krishna, M. Allen, J. Allen, E. Tutuc, D. Wasserman, Measurement of carrier lifetime in micron-scaled materials using resonant microwave circuits, Nat. Commun. 10 (1) (2019) 1–7.
- [26] S. Dev, Y. Wang, Y. Wang, M. Allen, J. Allen, E. Tutuc, D. Wasserman, Room temperature mid-infrared detection via resonant microwave circuits, IEEE Trans. Electron Dev. 67 (4) (2020) 1632–1638.
- [27] A.J. Noreika, J. Greggi Jr, W.J. Takei, M.H. Francombe, Properties of MBE grown InSb and InSb1 — x Bi x, J. Vacuum Sci. Technol. A: Vacuum, Surfaces, Films 1 (2) (1983) 558–561.
- [28] M. Zamiri, B. Klein, T. Schuler-Sandy, S. Myers, V. Dahiya, F. Cavallo, S. Krishna, Indium-bump-free antimonide superlattice membrane detectors on silicon substrates, Appl. Phys. Lett. 108 (9) (2016) 091110.
- [29] K. Kim, M. Yankowitz, B. Fallahazad, S. Kang, H.C. Movva, S. Huang, S. Larentis, C.M. Corbet, T. Taniguchi, K. Watanabe, S.K. Banerjee, B.J. LeRoy, E. Tutuc, van der Waals heterostructures with high accuracy rotational alignment, Nano Lett. 16 (3) (2016) 1989–1995.
- [30] J. Sun, J. Kosel, Room temperature inductively coupled plasma etching of InAs/ InSb in BCl3/Cl2/Ar, Microelectronic Eng. 98 (2012) 222–225.
- [31] https://www.analog.com/en/design-center/design-tools-and-calculators/ltspicesimulator.html (accessed on July 18, 2019).
- [32] B.V. Olson, C.H. Grein, J.K. Kim, E.A. Kadlec, J.F. Klem, S.D. Hawkins, E.A. Shaner, Auger recombination in long-wave infrared InAs/InAsSb type-II superlattices, Appl. Phys. Lett. 107 (26) (2015) 261104.
- [33] B.C. Connelly, G.D. Metcalfe, H. Shen, M. Wraback, C.L. Canedy, I. Vurgaftman, J.S. Melinger, C.A. Affouda, E.M. Jackson, J.A. Nolde, J.R. Meyer, E.H. Aifer, Investigation of trap states in mid-wavelength infrared type II superlattices using time-resolved photoluminescence, J. Electron. Mater. 42 (11) (2013) 3203–3210.